Wave Motion 147 (2026) 103785

Contents lists available at ScienceDirect

Wave Motion

journal homepage: www.elsevier.com/locate/wamot

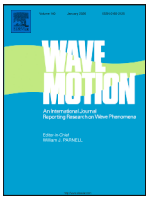

Large band gaps in artificial crystals tuned by constriction shape

David Röhlig*, Vincent Laude

Université Marie et Louis Pasteur, CNRS, institut FEMTO-ST, Besançon, 25000, France

ARTICLE INFO

Keywords:
Artificial crystal
Photonic crystal
Phononic crystal
Band structure
Band gaps
Finite element method (FEM)

ABSTRACT

It has been demonstrated - both numerically and experimentally - that constrictions arising in artificial crystals composed of touching impermeable inclusions can strongly inhibit the propagation of scalar waves, giving rise to wide complete band gaps. Building on this, we study the influence of the inclusion shape on the gap width when the contact points are preserved across different lattice types. The analysis reveals that the constriction geometry plays a decisive role in governing wave propagation; in effect, it acts as a tuning parameter for maximizing the band-gap width. Our findings may be taken into account for the design of future metamaterials.

1. Introduction

Since the inception of the field of artificial crystals, the emergence of band gaps - frequency ranges in which propagating waves become evanescent - has ranked among its most promising phenomena [1–3]. Conceptually, it reaches back to 1887 [4]; up to the present day, the search for wide complete band gaps has remained one of the central objectives. In subsequent decades, this research trajectory was shaped by optimization strategies based on topology and deep-learning techniques [5–7]. Early investigations already indicated that close packing of inclusions may promote the emergence of wide band gaps [8–10]; if the material contrast is sufficiently large, the dispersion relation may exhibit a flat-band character that enables gap opening [11–13]. This effect is maximized in crystals where local resonances are excluded by impermeable materials so that Bragg scattering remains to be the dominating mechanism [14]. This is why close packing has often been documented as optimal for sonic crystals where impermeability is approximated by a high material contrast between air and solid [8–10,13]. Despite these advantages, close-packed geometries have sometimes been avoided in practical implementations. Some reasons arise from methodological limitations: conventional plane-wave expansion techniques struggle to resolve the singular geometrical features associated with touching inclusions [15,16]. Other reasons stem from mechanical constraints - for instance, the structural fragility of plates perforated by densely packed holes [17]. Another example arises for water-wave crystals: when inclusions approach near contact, the flow through the narrow spaces between them becomes severely impeded; this cannot be covered within the framework of linear, inviscid, and irrotational wave theory as employed in ref. [18]. Moreover, wide gaps for close-packing systems have often been logically connected to the value of the filling fraction [8,10,17–20], defined as the ratio between the volume occupied by inclusions and the total volume of the unit cell.

In this paper, we instead emphasize that wide band gaps are favoured by the existence of constrictions. In previous investigations [13,14] we focussed on the existence of contact points and their effect, but not on the influence of the constriction shape. We show herewith that their geometry is actually essential for maximizing the band gap width even further. Under a controlled geometric framework, we compare all two-dimensional Bravais lattices under a common contact-point condition. We argue that spatial passages through which propagating waves have to make their way are optimal when they are narrow. The band gap systematically widens as these constrictions shrink.

* Corresponding author.
E-mail addresses: david.rohlig@femto-st.fr (D. Röhlig), vincent.laude@femto-st.fr (V. Laude).

https://doi.org/10.1016/j.wavemoti.2026.103785
Received 9 April 2026; Received in revised form 27 May 2026; Accepted 7 June 2026
Available online 10 June 2026

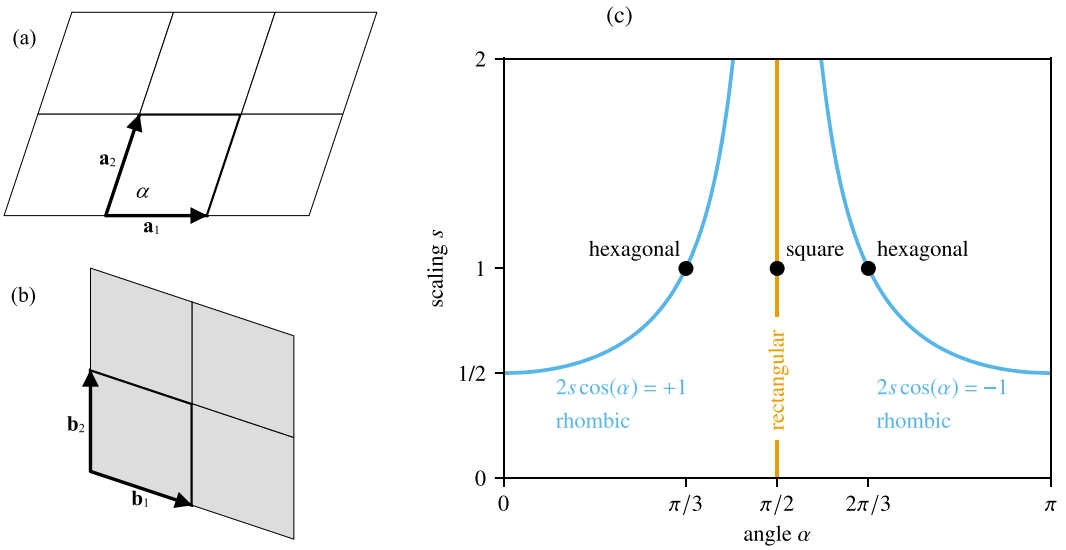

Fig. 1. The parametric definition of two-dimensional Bravais lattices, given in terms of (a) the primitive unit cell in direct space and (b) the primitive unit cell in reciprocal space. Panel (c) depicts the position of the five Bravais lattices within the parameter space defined by the scaling $s = a_2/a_1$ - representing the ratio of the magnitudes of the two basis vectors associated with the lattice constants a_1 and a_2 - and by the angle α between them. The most general configuration, exhibiting the lowest degree of symmetry, is the oblique lattice, which occupies almost all possible points in the diagram.

2. Lattice topology

In two dimensions, five Bravais lattices are distinguished, classified according to their symmetry properties. This standard convention, however, does not account for their respective prevalence in parameter space. Coordinates in two-dimensional lattices are measured along two non-aligned lattice vectors, $\mathbf{a}_1$ and $\mathbf{a}_2$, as depicted in Fig. 1(a). Given their magnitudes a_1 and a_2 as the lattice constants, we specifically set

$$\mathbf{a}_1 = a_1(1,0)^{\mathrm{T}} \tag{1}$$

$$\mathbf{a}_2 = a_2(\cos\alpha, \sin\alpha)^{\mathrm{T}} \tag{2}$$

These lattice vectors are connected by a scaling factor $s = a_2/a_1$ and the angle $\alpha \in]0, \pi[$ between them. This parametrization shows that any lattice can be continuously deformed into another within a parameter space of dimension two. In particular, the square lattice ($s = 1, \alpha = \pi/2$) with the highest degree of symmetry provides a convenient reference from which such deformations may be initiated. The reciprocal lattice vectors - depicted in Fig. 1(b) - define the first Brillouin zone; they are in turn

$$\mathbf{b}_1 = \frac{2\pi}{a_1 \sin\alpha}(\sin\alpha, -\cos\alpha)^{\mathrm{T}}, \tag{3}$$

$$\mathbf{b}_2 = \frac{2\pi}{a_2 \sin\alpha}(0,1)^{\mathrm{T}}. \tag{4}$$

Here, the scaling factor is $s = b_1/b_2$. The primitive unit cell in reciprocal space is thus continuously deformed from the square Brillouin zone. This relationship is illustrated in Fig. 1(c), which displays all possible configurations for two-dimensional lattices. Starting from the general case of the oblique lattice, symmetry enhancement may, for instance, be achieved by fixing the inter-vector angle to $\pi/2$, yielding the rectangular lattice, represented by the orange line. A further step is obtained by setting the scaling parameter s to unity, resulting in the square lattice. Moreover, by applying the condition $2s|\cos(\alpha)| = 1$, the lattice becomes centered rectangular, also referred to as rhombic. Finally, by imposing a more restrictive constraint on the angle ($\alpha = \pi/3$), one arrives at the hexagonal lattice.

3. Mesh quality for small constrictions

For our investigations, we must first define the considered close-packing artificial crystals. To allow for a fair comparison between the different lattice types, and given that the primitive unit cells have four sides, we impose the presence of four touching points defining four constrictions - one of which is located at the center of each side. Starting from the unit square lattice, any lattice defined by a doublet (s, α) can be generated by means of an affine transformation with the equation:

$$x' = a_1\, x + a_2 \cos(\alpha)\, y, \tag{5}$$

$$y' = a_2 \sin(\alpha)\, y. \tag{6}$$

Further, to enable an independent control of the inclusion shape, we introduce the following representation in polar coordinates:

$$x = r\,|\cos^{\beta-1}\theta|\cos\theta, \tag{7}$$

$$y = r\,|\sin^{\beta-1}\theta|\sin\theta, \tag{8}$$

where the exponent β effectively controls the shape and the radius $r = a_1/2$. In particular, $\beta = 1$ yields the circular case, whereas $\beta = 2$ produces a rotated square inclusion; intermediate values such as $\beta = 1.5$ provide a continuous transition between these inclusion shapes. In order to obtain the numerical results in our study of close-packing artificial crystals, we used the finite element method as thematized later. Fig. 2(a) displays these four cases for a square lattice crystal of impermeable inclusions. It becomes clear that the constrictions progressively narrow as the parameter β decreases. In all cases, the mesh is divided into four parts connected by a single point. When the affine transform is applied to the mesh, this connectivity property remains: the contact points sit exactly in the middle of each side. As a consequence, the inclusion undergoes a deformation - as do the resulting constrictions around the contact points. The examples shown in Fig. 2(b) illustrate the transformation toward a hexagonal lattice corresponding to the four values of β considered in Fig. 2(a).

In order to resolve the constriction shape with sufficient accuracy, mesh adaptation becomes necessary. As a rule, the convergence of the band structures may be enhanced by a denser sampling near the contact points, whereas sampling can be relaxed away from them. One conceivable strategy could be the use of mesh adaption based on an estimate of the finite element solution quality. However, we have found this approach to be made difficult by the connectivity of the mesh at the contact points. We therefore adopted a geometrical approach: the sampling along the boundaries of the mesh is gradually increased when approaching the midpoint of a side. For the square lattice, characterised by a single lattice constant $a = a_1 = a_2$, the sampling density $t \in [0, a/2]$ along one half of a unit-cell edge was varied according to

$$t' = \frac{a}{2}\frac{\tanh\left(\frac{2\gamma_1 t}{a}\right)}{\tanh(\gamma_1)}. \tag{9}$$

Here, t and t' denote curvilinear coordinates along the respective half edge; t is sampled uniformly, whereas γ_1 represents a constant controlling the local mesh density; it was set to three in the examples presented below. Similarly, the internal circular boundary is partitioned at the contact points; the four resulting sectors are sampled in a non-uniform manner. For instance, the sector defined by $\theta \in [-\pi/4, \pi/4]$ is sampled according to

$$\theta' = \frac{\pi}{4}\frac{\tanh\left(\frac{4\gamma_2\theta}{\pi}\right)}{\tanh(\gamma_2)}. \tag{10}$$

γ_2 again denotes a constant controlling the local mesh density; it equals two in the provided examples.

4. Results

After the construction of the mesh, we proceed to solve for the band structures of the different lattices. Following ref. [14], we consider the Helmholtz equation and solve its weak form with the finite element method (see Appendix A for a description); computations are performed using FreeFem++ [21]. To model our structures, we assumed a single-phase material and impermeable inclusions in which resonances are excluded. This case encompasses many different scalar wave equations for acoustics, plasmonics, photonics, or water waves. Given that there is a single material wave velocity, noted c, we can consider reduced frequencies defined as $f = \omega a_1/2\pi c$. As a note, we have $f = a_1/\lambda$ with λ the wavelength in the base material. Band structures for close-packing crystals have already been provided in refs. [13] and [14] and are not repeated here. In short, it was observed that the bands are very flat, delimiting very wide band gaps. The lowest band, in particular, spans frequencies from zero up to $f_1 > 0$, marking the entrance of the first Bragg gap; the subsequent band closes the first Bragg gap at the frequency f_2. Since our primary interest lies in the width of the first Bragg gap, we evaluate it directly from the density of states (DOS), which is obtained by uniformly sampling the first Brillouin zone. Conventionally, we measure this width by means of the band gap width (BGW) metric defined as

$$\mathrm{BGW} = 2\frac{f_2 - f_1}{f_2 + f_1}. \tag{11}$$

With the frequency bounds introduced above for f_1 and f_2, this metric is constrained to the interval $[0, 2]$. The upper bound is attained for $f_1 = 0$, irrespective of the value of f_2.

Let us first compare crystals with a scaling of $s = 1$, and $\beta = 1$ for circular inclusions. Fig. 3(a) displays the DOS for the cases $\alpha = \pi/2$ (square lattice), $\alpha = \pi/3$ (hexagonal lattice), and an intermediate configuration, $\alpha = 5\pi/12$ (oblique lattice). All three DOS curves are composed of sharp peaks marking the flat bands. The first peak defining f_1 is almost the same for all three values of α, but f_2 is clearly larger for the square lattice. The first peak defining f_1 remains nearly identical for all three values of α, whereas f_2 is distinctly larger for the square lattice. These characteristics have already been verified experimentally for both the square [13,14] and the hexagonal lattice [14], although the presented band gaps in those references are less pronounced owing to limitations in fabrication precision. Second, we examine crystals with $s = 1.2$ and circular inclusions ($\beta = 1$). Fig. 3(b) shows the DOS for the cases $\alpha = \pi/2$ (rectangular lattice), $\alpha = \pi/3$ (oblique lattice), and $2\,s\cos(\alpha) = 1$ (rhombic lattice). As in the preceding analysis, f_1 varies insignificantly; by contrast, f_2 decreases continuously away from condition $\alpha = \pi/2$.

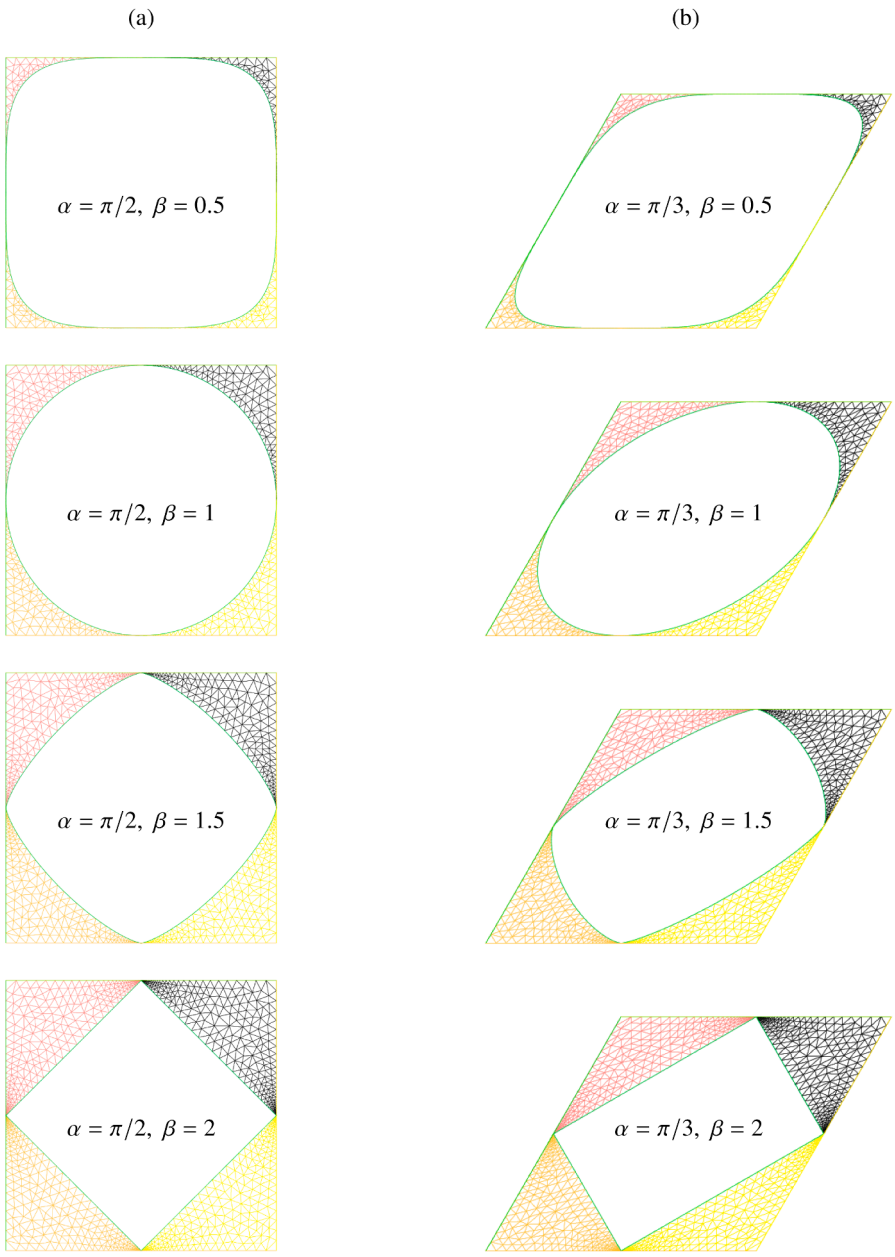

Fig. 2. Finite-element meshes obtained for $s = 1$ and different values of the parameter β, which controls the inclusion shape. The left column (a) corresponds to a square-lattice crystal ($\alpha = \pi/2$), whereas the right column (b) depicts hexagonal lattices ($\alpha = \pi/3$). The mesh resolution is chosen such that 80 nodes are distributed along each external border.

Table 1 summarizes the calculated BGW obtained for the different close-packing crystals considered in this study. Varying the lattice type changes the band-gap width - which appears to attain its maximum for the square lattice. The entrance frequency f_1 of the Bragg-gap approaches zero, whereas the exit frequency f_2 lies close to the maximal unit value. In this respect, the conventional BGW metric hardly captures the differences between lattices. Notably, compared to the lattice type, the constriction shape exerts an even stronger influence on the width, as Fig. 4 illustrates. For the square lattice (see Fig. 4(a)), transforming the inclusion from a circular to a square by increasing the value of β, enhances band dispersion and narrows the complete band gaps. Fig. 4(b) confirms this behaviour for the hexagonal lattice; it can be explained as follows: For low values of β, the constriction becomes narrow. By contrast, when β is increased the constriction elongates and gives rise to a narrow tunnel-like region surrounding the contact points. Propagating waves are then compelled to traverse the confined path, which drastically reduces the group velocity. As a consequence, the eigensolutions become concentrated within sharply defined frequency intervals and complete band gaps widen.

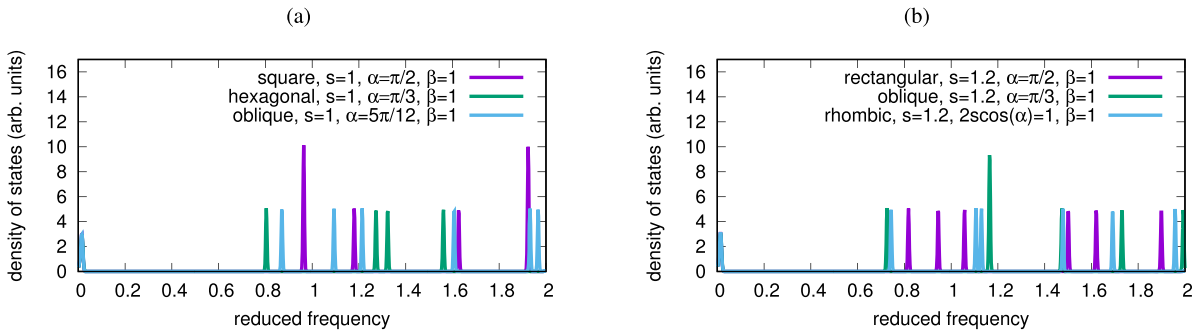

Fig. 3. Influence of the Bravais lattice type on the density of states: (a) for a scaling factor $s = 1$ and (b) for $s = 1.2$.

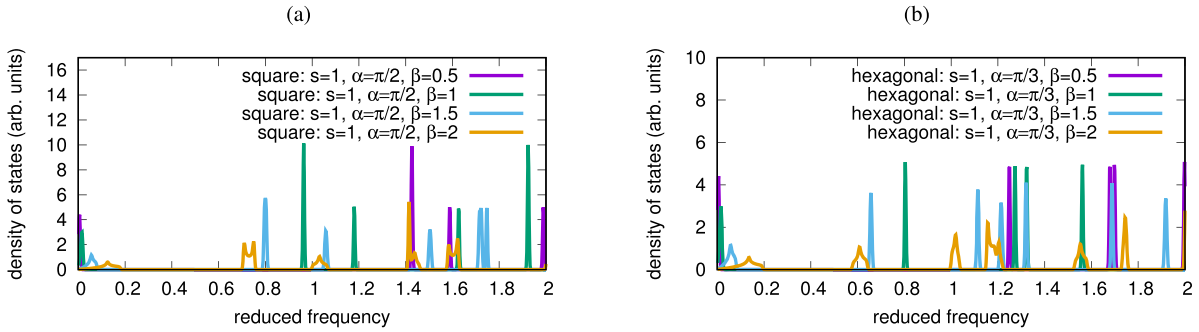

Fig. 4. Influence of the constriction shape on the density of states: (a) for the square lattice with $\alpha = \pi/2$ and (b) for the hexagonal lattice with $\alpha = \pi/3$. The scaling factor is fixed at $s = 1$, while the exponent β is varied.

Table 1
Entrance and exit reduced frequencies, as well as the band-gap width (BGW), for the various artificial crystals considered in Figs. 3 and 4.

s	α	β	f_1	f_2	BGW	lattice type
1.0	$\pi/2$	1.0	0.021	0.963	1.91	square
1.0	$\pi/3$	1.0	0.021	0.805	1.90	hexagonal
1.0	$5\pi/12$	1.0	0.022	0.871	1.90	oblique
1.2	$\pi/2$	1.0	0.021	0.817	1.90	rectangular
1.2	$\pi/3$	1.0	0.022	0.725	1.88	oblique
1.2	$\cos^{-1}(\frac{1}{2s})$	1.0	0.020	0.744	1.90	rhombic
1.0	$\pi/2$	0.5	0.008	1.427	1.98	square
1.0	$\pi/2$	1.5	0.080	0.796	1.63	square
1.0	$\pi/2$	2.0	0.182	0.706	1.18	square
1.0	$\pi/3$	0.5	0.010	1.250	1.97	hexagonal
1.0	$\pi/3$	1.5	0.080	0.654	1.56	hexagonal
1.0	$\pi/3$	2.0	0.194	0.577	0.99	hexagonal

5. Discussion

In summary, we characterised the two-dimensional lattice types by two continuous parameters: the angle α and the scale s. By varying these parameters, a square primitive unit cell can be continuously transformed into the one associated with any other lattice. In addition, we introduced the parameter β that controls the shape of the inclusion. In the computations, the mesh must be carefully constructed to capture the effect of a small constriction around a contact point. Results for the densities of states confirm the formation of exceptionally wide band gaps for all five Bravais lattices. In case of four constrictions per unit cell, the square lattice performs best among the presented lattice types. More importantly, the results indicate that - beyond the mere existence of contact points, the geometric shape of the constrictions formed by the inclusions exerts a decisive influence on band-gap formation. Indeed, this factor may prove at least as significant as the lattice type itself; it dictates wave dispersion inside the crystal. To conclude, the mere existence of contact points does not, in itself, exhaust the full picture; rather, the resulting dispersion characteristics are determined by the manner in which waves propagate through the constrictions formed by impermeable inclusions. In order to maximize the

band-gap widths, the waves must be forced to traverse sufficiently narrow channels, and the constrictions should therefore be designed accordingly. This observation may serve as a guiding principle for the development of future metamaterials.

CRediT authorship contribution statement

David Röhlig: Writing – review & editing, Writing – original draft, Visualization, Validation, Software, Methodology, Investigation, Formal analysis, Data curation, Conceptualization; **Vincent Laude:** Writing – review & editing, Writing – original draft, Visualization, Validation, Supervision, Software, Resources, Project administration, Methodology, Investigation, Funding acquisition, Formal analysis, Data curation, Conceptualization.

Data availability

Data will be made available on request.

Declaration of competing interest

The authors declare that they have no known competing financial interests or personal relationships that could have appeared to influence the work reported in this paper.

Acknowledgments

The authors acknowledge support by the EIPHI Graduate school (contract “ANR-17-EURE-0002”) and by the Bourgogne-Franche-Comté Region.

Appendix A. Finite element formulation

We consider a generic Helmholtz equation with a single material in the unit cell that contains an impermeable inclusion solely defined by a Neumann boundary condition [14]. Its weak form is solved using the finite element method on the meshes exemplified in Fig. 2. We consider the strong form of the Helmholtz equation as

$$\triangle u(\boldsymbol{r}) + \frac{\omega^2}{c^2} u(\boldsymbol{r}) = 0, \tag{A.1}$$

where ω denotes the angular frequency, c the wave speed and u represents the wave field. Introducing Bloch waves $u(\boldsymbol{r}, t) = \tilde{u}(\boldsymbol{r}) \exp(i\omega t - i\boldsymbol{k} \cdot \boldsymbol{r})$ for both the field and the test function $v(\boldsymbol{r}, t)$, the weak form has the form of an eigenvalue problem

$$\frac{\omega^2}{c^2} \int_\Omega \tilde{v^*}\, \tilde{u}\, \mathrm{d}\boldsymbol{r} = \int_\Omega (\nabla + i\boldsymbol{k})\tilde{v^*} \cdot (\nabla - i\boldsymbol{k})\tilde{u}\, \mathrm{d}\boldsymbol{r} \tag{A.2}$$

Both integrals are defined over the whole unit cell domain Ω, which consists of a single material. The function $\tilde{u}(\boldsymbol{r})$ has the periodicity of the lattice. For real wavevectors the second integral defines a Hermitian-symmetric matrix, hence real and positive eigenvalues ω^2/c^2, and orthogonal eigenvectors.

Appendix B. Brillouin zone sampling and density of states

As described in Section 2, the primitive unit cell in reciprocal space, parametrizing the first Brillouin zone, is a parallelogram with basis vectors $\mathbf{b}_1$ and $\mathbf{b}_2$. One quarter of this reciprocal unit cell is sampled using the N^2 discrete wavevectors

$$\mathbf{k}[n_1, n_2] = \frac{n_1}{N-1}\frac{\mathbf{b}_1}{2} + \frac{n_2}{N-1}\frac{\mathbf{b}_2}{2}, \quad n_1, n_2 \in [0, N-1]^2 \tag{B.1}$$

For the computations presented in the manuscript, $N = 31$, such that the reciprocal unit cell is sampled with 961 k-points. Owing to symmetry, it suffices to sample only one quarter of the reciprocal unit cell - for instance, the upper-right quadrant. Note that the usual high symmetry points of the first Brillouin zone are all automatically included. Solving the eigenvalue problem for the N^2 wavevectors yields a set of reduced eigenfrequencies $f[n_1, n_2, q]$, with $q \in [1, Q]$ labelling the discrete Bloch bands ($Q = 16$ eigenvalues are computed for each wavevector). The density of states is then defined as a continuous function of reduced frequency as follows.

$$h(f) = \sum_{n_1=0}^{N-1} \sum_{n_2=0}^{N-1} \sum_{q=1}^{Q} \frac{1}{2\pi\, \delta f} \exp\left(-\frac{(f - f[n_1, n_2, q])^2}{2\, \delta f^2} \right). \tag{B.2}$$

Within complete band gaps, we have $h(f) = 0$; thus, this condition makes it easy to identify the reduced entrance and exit frequencies of complete band gaps, in particular f_1 and f_2 as listed in Table 1. In order to plot Figs. 3 and 4, we have used $\delta f = 0.003$.

Appendix C. Solver settings and convergence

All finite element computations and meshing operations are performed using `FreeFem++` [21]. The finite element matrices are constructed with quadratic Lagrange elements. We select the direct eigenvalue solver `Arpack` that is designed to compute a few eigenvalues and the corresponding eigenvectors of large sparse or structured matrices. For symmetric matrices, `Arpack` implements the Lanczos algorithm. Convergence in this case is known to occur from above, so that the eigenfrequencies are systematically overestimated. In the case of constrictions, the limiting element for convergence is the part of the mesh that surrounds the contact point and convergence is slower as parameter β decreases, i.e. as the constriction becomes less wide. The straight boundaries of the mesh, extending between a corner and a contact point, are sampled using $n_h = 40$ vertices; the curved boundaries between two contact points are sampled using $\lceil \pi\, n_h/2 \rceil = 63$ vertices, where $\lceil \cdot \rceil$ denotes the ceiling function. This meshing resolution was verified to yield an accuracy better than 0.5% for the reduced frequencies reported in Table 1.

Appendix D. Examples of band structures

Fig. D.5 displays two exemplar band structures, for illustration of the impact of the shape of the inclusion near contact points. In case of a narrow constriction ($\beta = 0.5$), the band structure is composed only of very flat bands separated by giant band gaps. In the opposite case of a wide constriction ($\beta = 2$), bands are comparatively less dispersive and the complete band gaps comparatively smaller.

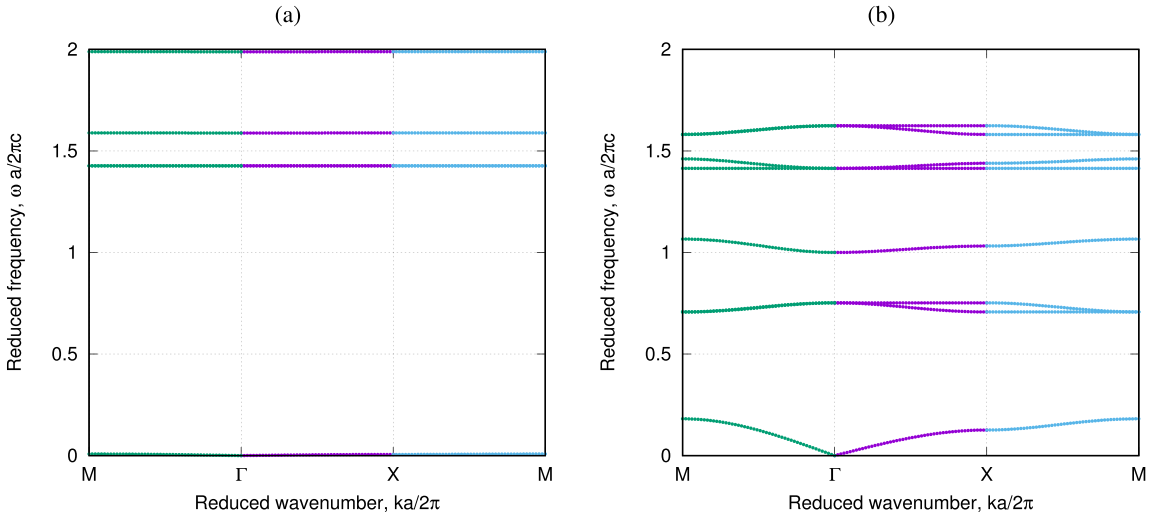

Fig. D.5. Band structures for square lattice crystals ($s = 1$, $\alpha = \pi/2$) with touching empty inclusions for (a) $\beta = 0.5$ and (b) $\beta = 2$. The corresponding meshes are displayed in Fig. 2(a).

References

[1] J. Maddox, Photonic band-gaps bite the dust, Nature 348 (6301) (1990) 481. https://doi.org/10.1038/348481a0
[2] E. Yablonovitch, Photonic band-gap crystals, J. Phys.: Condens. Matter 5 (16) (1993) 2443. https://doi.org/10.1088/0953-8984/5/16/004
[3] M.S. Kushwaha, P. Halevi, L. Dobrzynski, B. Djafari-Rouhani, Acoustic band structure of periodic elastic composites, Phys. Rev. Lett. 71 (1993) 2022–2025. https://doi.org/10.1103/PhysRevLett.71.2022
[4] L. Rayleigh, XVII. On the maintenance of vibrations by forces of double frequency, and on the propagation of waves through a medium endowed with a periodic structure, Lond. Edinb. Dublin Philos. Mag. J. Sci. 24 (147) (1887) 145–159. https://doi.org/10.1080/14786448708628074
[5] O. Sigmund, J. Søndergaard Jensen, Systematic design of phononic band-gap materials and structures by topology optimization, Philosoph. Transact. Roy. Soc. Lond. Ser. A: Math. Phys. Eng. Sci. 361 (1806) (2003) 1001–1019. https://doi.org/10.1098/rsta.2003.1177
[6] J.S. Jensen, O. Sigmund, Topology optimization for nano-photonics, Laser Photon. Rev. 5 (2) (2011) 308–321. https://doi.org/10.1002/lpor.201000014
[7] J. Li, M. Qian, J. Yin, W. Lin, Z. Zhang, S. Liu, Topology design of soft phononic crystals for tunable band gaps: a deep learning approach, Materials 18 (2) (2025). https://doi.org/10.3390/ma18020377
[8] D. Caballero, J. Sánchez-Dehesa, C. Rubio, R. Mártinez-Sala, J.V. Sánchez-Pérez, F. Meseguer, J. Llinares, Large two-dimensional sonic band gaps, Phys. Rev. E 60 (1999) R6316–R6319. https://doi.org/10.1103/PhysRevE.60.R6316
[9] P. Lambin, A. Khelif, J.O. Vasseur, L. Dobrzynski, B. Djafari-Rouhani, Stopping of acoustic waves by sonic polymer-fluid composites, Phys. Rev. E 63 (2001) 066605. https://doi.org/10.1103/PhysRevE.63.066605
[10] M.S. Kushwaha, Stop-bands for periodic metallic rods: sculptures that can filter the noise, Appl. Phys. Lett. 70 (24) (1997) 3218–3220. https://doi.org/10.1063/1.119130
[11] Y. Liang, G. Yun, H. Yang, N. Bai, Y. Cao, Dirac points and flat bands in two-dimensional magnonic crystals with honeycomb-kagome structure, AIP Adv. 14 (3) (2024) 035242.
[12] D. Röhlig, E. Kuhn, F. Teichert, A. Thränhardt, T. Blaudeck, Function phononic crystals, Europhys. Lett. 145 (2) (2024) 26001. https://doi.org/10.1209/0295-5075/ad1de9

[13] D. Röhlig, A. Thränhardt, V. Laude, T. Blaudeck, Giant band gaps in a phononic crystal with touching solid inclusions, Phys. Rev. Appl. 23 (2025) 054055. https://doi.org/10.1103/PhysRevApplied.23.054055
[14] D. Röhlig, R. Zichner, T. Blaudeck, A. Thränhardt, V. Laude, Contact points open wide band gaps in all two-dimensional Bravais lattices, Phys. Rev. B 113 (2026) 144319. https://doi.org/10.1103/9ql7-t9rh
[15] L. Li, Use of Fourier series in the analysis of discontinuous periodic structures, J. Opt. Soc. Am. A 13 (9) (1996) 1870–1876. https://doi.org/10.1364/JOSAA.13.001870
[16] H.S. Sözüer, J.W. Haus, R. Inguva, Photonic bands: convergence problems with the plane-wave method, Phys. Rev. B 45 (1992) 13962–13972. https://doi.org/10.1103/PhysRevB.45.13962
[17] S. Mohammadi, A.A. Eftekhar, A. Khelif, A. Adibi, Simultaneous two-dimensional phononic and photonic band gaps in opto-mechanical crystal slabs, Opt. Express 18 (9) (2010) 9164–9172. https://doi.org/10.1364/OE.18.009164
[18] X. Hu, C.T. Chan, Refraction of water waves by periodic cylinder arrays, Phys. Rev. Lett. 95 (2005) 154501. https://doi.org/10.1103/PhysRevLett.95.154501
[19] C.M. Reinke, M.F. Su, R.H. Olsson, III, I. El-Kady, Realization of optimal bandgaps in solid-solid, solid-air, and hybrid solid-air-solid phononic crystal slabs, Appl. Phys. Lett. 98 (6) (2011) 061912. https://doi.org/10.1063/1.3543848
[20] J.-J. Liu, Z.-G. Fan, H.-S. Xiao, W. Zhang, C.-Y. Guan, L. Yuan, Photonic band gap in Ge-based two-dimensional triangular lattice photonic crystals, J. Infrared Millim. Wave. 31 (2012) 35–41. https://doi.org/10.3724/SP.J.1010.2012.00035
[21] F. Hecht, New development in freefem++, J. Numer. Math. 20 (3–4) (2012) 251–266. https://freefem.org/. https://doi.org/10.1515/jnum-2012-0013